Variation in Upper Plate Crustal and Lithospheric Mantle Structure in the Greater and Lesser Antilles from Ambient Noise Tomography

D. Schlaphorst[1,2], N. Harmon[3], J.M. Kendall[4], C.A. Rychert[3], J. Collier[5], A. Rietbrock[6], S. Goes[5], and the VoiLA Team[†]

†The VoiLA Team:

R.W. Allen[5], L. Bie[6], J.D. Blundy[4], B. Chichester[3], G.F. Cooper[7], J.P. Davidson[8], R.G. Davy[5], T.J. Henstock[3], S.P. Hicks[5], C.G. Macpherson[8], B. Maunder[5], J. Prytulak[8], J. van Hunen[8], J.J. Wilkinson[5,9], M. Wilson[10]

[1]Instituto Dom Luiz (IDL), Universidade de Lisboa, Portugal.

[2]School of Earth Sciences, University of Bristol, UK.

[3]Ocean and Earth Science, University of Southampton, National Oceanography Centre, Southampton, UK.

[4]Department of Earth Sciences, University of Oxford, UK.

[5]Department of Earth Science and Engineering, Imperial College London, London, UK.

[6]Geophysical Institute (GPI), Karlsruhe Institute of Technology, Karlsruhe, Germany.

[7]School of Earth and Environment, Cardiff University, Cardiff, UK

[8]Department of Earth Sciences, Durham University, Durham, UK.

[9]Department of Earth Sciences, Natural History Museum, London, UK.

[10]School of Earth and Environment, University of Leeds, Leeds, UK.

Corresponding author: David Schlaphorst (dschlaphorst@fc.ul.pt)

Key Points:

- With land and ocean bottom seismometers, we map significant variations in sediment/crustal thickness in fore- and back-arc in new detail.
- Sediments thickens towards the southern arc, whereas crustal thickness increases towards the north.
- Volatile input and pathways depend on slab seafloor morphology, 3D flow and/or melt ponding beneath the upper plate redistributing melt.

Abstract

The crust and upper mantle structure of the Greater and Lesser Antilles Arc provides insights into key subduction zone processes in a unique region of slow convergence of old slow-spreading oceanic lithosphere. We use ambient noise tomography gathered from island broadband seismic stations and the temporary ocean bottom seismometer network installed as part of the VoiLA experiment to map crustal and upper mantle shear-wave velocity of the eastern Greater Antilles and the Lesser Antilles Arc. Taking the depth to the 2.0 km/s contour as a proxy, we find sediment thickness up to 15 km in the south in the Grenada and Tobago basins and thinner sediments near the arc and to the north. We observe thicker crust, based on the depth to the 4.0 km/s velocity contour, beneath the arc platforms with the greatest crustal thickness of around 30 km, likely related to crustal addition from arc volcanism through time. There are distinct low velocity zones (4.2-4.4 km/s) in the mantle wedge (30-50 km depth), beneath the Mona Passage, Guadeloupe-Martinique, and the Grenadines. The Mona passage mantle anomaly may be related to ongoing extension there, while the Guadeloupe-Martinique and Grenadine anomalies are likely related to fluid flux, upwelling, and/or partial melt related to nearby slab features. The location of the Guadeloupe-Martinique anomaly is slightly to the south of the obliquely subducted fracture zones. This feature could be explained by either three-dimensional mantle flow, a gap in the slab, variable slab hydration, and/or melt dynamics including ponding and interactions with the upper plate.

1 Introduction

Subduction zones play a key role in driving plate tectonics, delivering slabs and their volatile elements to the mantle. Slab dehydration during the subduction process results in melt generation, which rises and eventually leads to the formation of volcanic island arcs. Hydration may vary along strike depending on slab crustal structure, fracture zones and sediment packages (Stern, 2003). However, the relative importance of these delivery mechanisms and the exact pathways of hydration and melt to surface volcanism are not well known. Imaging variations in the crust and lithospheric mantle in these regions offers insights into subduction processes and the formation of continental crust through arc volcanism. Seismic methods offer the best potential to image the arc lithosphere at the scale of tens of kilometres required. However, many studies of island arcs are limited by the restriction of land stations to mostly small arc islands (noisy) in a linear alignment or sparsity in linear offshore active-source seismic profiles. A further limitation on our understanding of subduction processes is that until recently, seismic studies have focussed mostly on Pacific subduction zones (see Melekhova et al. (2019) for lists of references). The Volatile Recycling in the Lesser Antilles (VoiLA) experiment is focussed on the Lesser Antilles Arc (LAA), where slow-spread lithosphere are subducted (Goes et al., 2019).

Many subduction zones show complex crust and mantle structure in the upper plate, with along-arc heterogeneities, such as mantle xenolith mineral composition and discontinuity depths (e.g., Boynton et al., 1979; Kodaira et al., 2007; Melekhova et al., 2019; Schlaphorst et al., 2018; Shillington et al., 2004). These are likely related to factors including variation in slab age, convergence rate and direction. In addition, it is likely that oceanic plates are more hydrated at slow spreading centres that at fast spreading centres (e.g., Davy et al., 2019) and the distribution of hydration can vary significantly along the arc (e.g., Schlaphorst et al., 2016). Related to that, erupted magmas from Guadeloupe and Dominica show a high $\delta^{11}B$ anomaly that is indicative of

dewatering of serpentinized oceanic crust (Cooper et al., 2020). In recent years, differences in the nature and intensity of the aforementioned slab heterogeneities between regions of subduction of fast spreading plates (mostly located in the Pacific) and those of slow spreading plates (found in the Atlantic) have become increasingly clear (Bie et al., 2020; Cooper et al., 2020; Melekhova et al., 2019; Schlaphorst et al., 2018).

Here, we image the LAA and the eastern Greater Antilles (GA), a slow-subduction zone located at the eastern boundary of the Caribbean plate, using ambient noise tomography (ANT). ANT has been used in a recent study to map shear-wave velocities in the Caribbean (Arnaiz-Rodríguez et. al, 2020). In our study, data are recorded by a dense network of permanent land stations and additionally an array of oceanic bottom seismometers deployed during the VoiLA experiment (VoiLA; Goes et al., 2019), which increases resolution in the fore- and back-arc. Previous studies have investigated the crustal structure in this area via active source imaging and receiver functions (e.g., Allen et al., 2019; Arnaíz-Rodroguez et al., 2016; Boynton et al., 1979; Chichester et al. , 2020; Christeson et al., 2008; Dorel et al, 1974; Kopp et al., 2011; Melekhova et al., 2019; Pauldron et al., 2020; Schlaphorst et al., 2018; Sevilla et al., 2012) but the inter-island subsurface is poorly studied so far. Our aim is to image the shallow mantle and crust, investigating variations in sediment accumulation, crustal thickness and the velocity structure in the uppermost mantle across the arcs.

2 Tectonic Setting

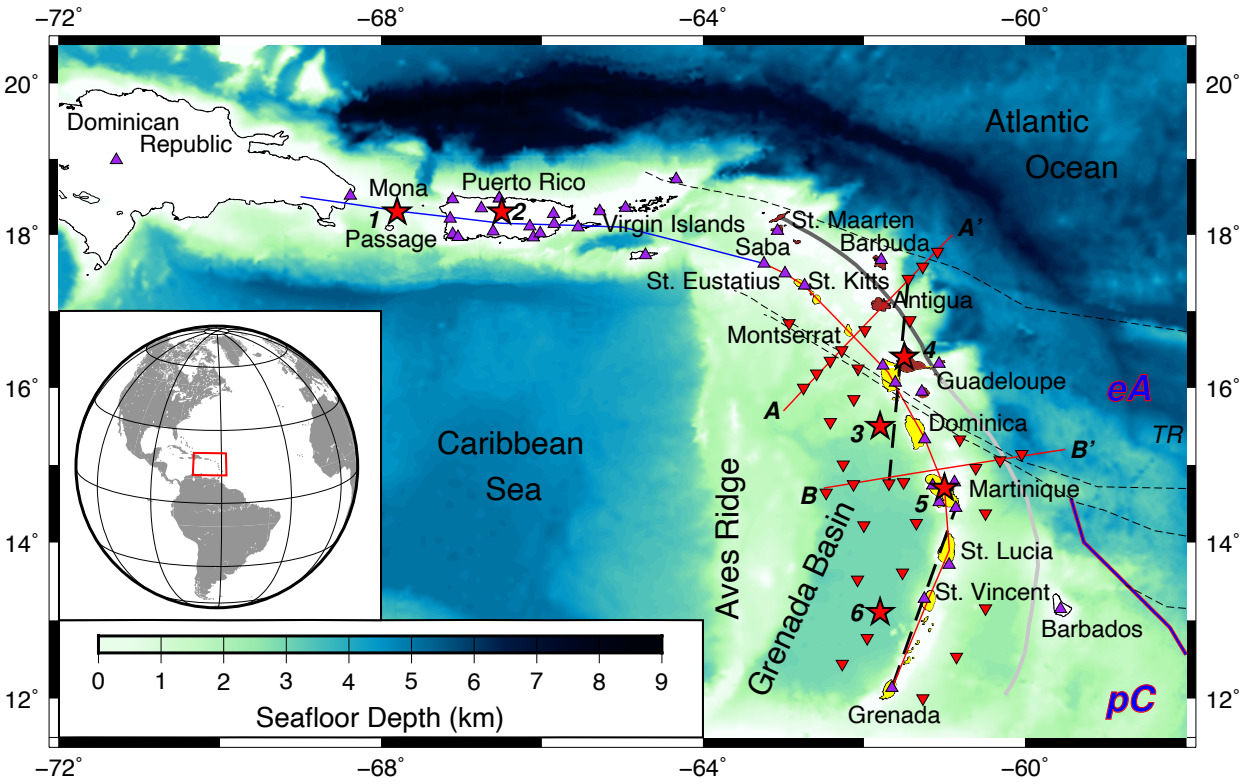

Figure 1: Map of the LAA and the GA, including bathymetry and the locations of seismic island stations (purple triangles) and OBS stations (red inverted triangles). Station details can be found in Supplementary Table S1. The global location of the area is shown in the inset. The islands of the LAA are coloured in yellow (Volcanic Caribbees) and brown (Limestone Carribees), and the islands of the GA are white. The location of the outer arc is shown as a thick grey line with the southern buried part depicted in a lighter grey (Allen et al., 2019). Thin black dashed lines indicate fracture zones and the purple show the boundary between the proto-Caribbean (pC) and equatorial Atlantic (eA) seafloor (Cooper et al., 2020). TR indicates the start of the Tiburon Ridge. Thick black hashed lines indicate the paths of the cross-correlated data from island–island and OBS–OBS station pairs for the examples shown in Fig. 3. Red stars show the locations of the individual results (Fig. 8). Thin solid lines indicate positions of the cross-sections (Fig. 10) for the GA (blue) and LAA (red).

The eastern GA and LAA (Fig. 1) are located on the northern and eastern margin of LIP-thickened (large igneous province) oceanic crust of the Caribbean plate (Mauffret & Leroy, 1997). The origin and evolution of the Caribbean plate since the Cretaceous can be inferred from its crustal structure. Over the past 100 My the Caribbean plate has been moving eastwards relative to both the North and South American plates. This motion has been accommodated by subduction, and strike-slip boundaries, resulting in large-scale shear zones through continental/oceanic crust and arc volcanism at various times and places on the plate margin

(Boschman 2014). Subsequently, sedimentation and tectonism have obscured many of these features, therefore making it difficult to unravel a complex history.

The eastern GA area includes the islands of Hispaniola, Puerto Rico and the Virgin Islands, which together form the Northern Caribbean Plate Boundary Zone. The islands are located on microplates, which override the North American Plate and the thickened Caribbean Plate in two subduction zones to the north and to the south (Dolan et al., 1998). Dominated by a left-lateral, east-west strike-slip motion, the complex tectonic setting of the area includes oblique convergence of the North American Plate, as well as a pull-apart basin in the Mona Passage between Hispaniola and Puerto Rico (Dolan et al., 1998; Masson & Scanlon, 1991; Ten Brink, 2005). Furthermore, a potential slab gap east of Puerto Rico has been suggested in several studies, based on bathymetry, seismic reflection profiles and gravity measurements (Ten Brink, 2005), as well as shear-wave splitting (Meighan et al., 2013; Schlaphorst et al., 2017).

The volcanic islands of the LAA have been formed by slow (18 to 20 mm/yr; DeMets et al., 2000), westward subduction of the North and South American plates beneath the Caribbean Plate (Wadge & Shepherd, 1984). The entire arc extends about 800 km in a mostly north-south orientation. To the north and south it is bound by the GA and the South American continent, respectively. To the west it neighbours the Grenada Basin and the Aves Ridge (Boynton et al., 1979; Christeson et al., 2008), an abandoned, Mesozoic volcanic arc. The Grenada Basin forms a depression characterised by a flat bottom in the south with depths down to 3 km that spans a region of roughly 150 by 600 km along the curved outline of the LAA and has formed due to north-south striking back-arc spreading while the so-called outer arc (OA; Fig. 1) was active (Allen et al., 2019; Bouysse, 1988; Padron et al., 2020).

The surface expression of the present-day arc comprises eleven major islands and the smaller Grenadine islands between St. Vincent and Grenada. Due to a spatial and temporal variations in magmatic output, the size and spacing of the volcanic islands varies. Around the island of Dominica, the LAA bifurcates to the north: the western active limb (the Volcanic Caribbees) includes the western part of Guadeloupe, as well as Montserrat, St. Kitts, St. Eustatius and Saba; the inactive eastern limb (the Limestone Caribbees) includes the eastern part of Guadeloupe, as well as Antigua, Barbuda and St. Martin (Bouysse et al., 1990). The Limestone Caribbees are part of the old OA that continues to the south buried under sediments from the Barbados accretionary prism (Allen et al., 2019). Due to the curvature of the present-day arc, a systematic change in subduction style can be observed, with increased strike-slip movement towards the northern end (DeMets et al., 1994, 2000). A further variation along the arc includes the sedimentary load of the incoming plate. Northward extent of sediment on the incoming plate sourced from the South America continent is blocked by the presence of the east-west trending Tiburon Ridge and other submarine highs leading to thicker sediment cover in the south relative to the north.However, it is possible that a major part of these clastic sediments is accreted rather than subducted, forming the Barbados accretionary prism (e.g., Faugères et al., 1993). The orientation of the Wadati-Benioff zone along the arc also shows a significant change and thickens towards the south. The top of the subducting slab can be inferred from seismicity, lying at a depth of roughly 120 km beneath the islands of the LAA (Bie et al., 2020). Finally, there is a change in the age and origin of the plate along strike, with the proto-Caribbean lithosphere subducting ahead of the South American oceanic lithosphere south of Dominica and

157 lithosphere generated at the Mid-Atlantic Ridge (MAR) subducting to the North (Cooper et al.,
158 2020).

159

3 Approach and Method

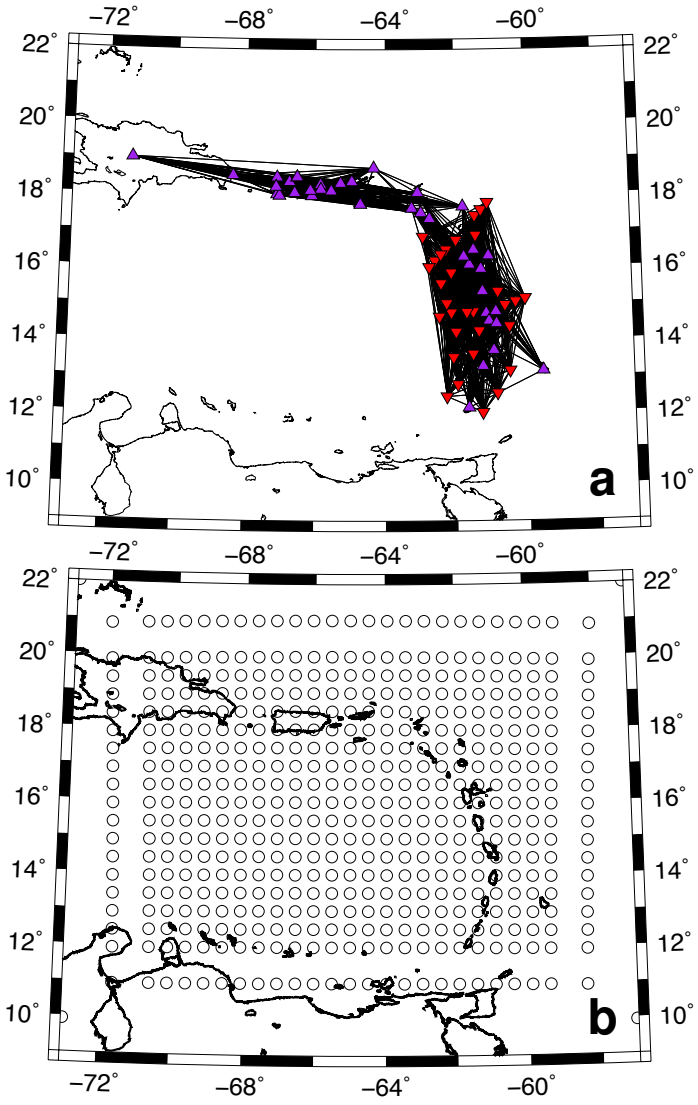

Figure 2: Station pairs and nodal parameterisation. a) Map showing the station pairs used, including locations of seismic island stations (purple triangles) and OBS stations (red inverted triangles). Note that due to the addition of OBS stations the tomography can be carried out on a broader range in the LAA. Moreover, we did not include station pairs between the GA and the LAA, since no crossing paths were possible. b) Nodal parameterisation used in this study with nodes being indicated by the white circles. The spacing is 0.5˚ by 0.5˚. The outside nodes are placed at a 1˚ distance and are included to dampen any potential heterogeneity outside the region of interest. Nodes exist across the Caribbean Sea where we do not expect data recovery owing to the setup of the code. As there is no sensitivity to these nodes due to lack of station-to-station paths, this does not have a negative effect on the resolution.

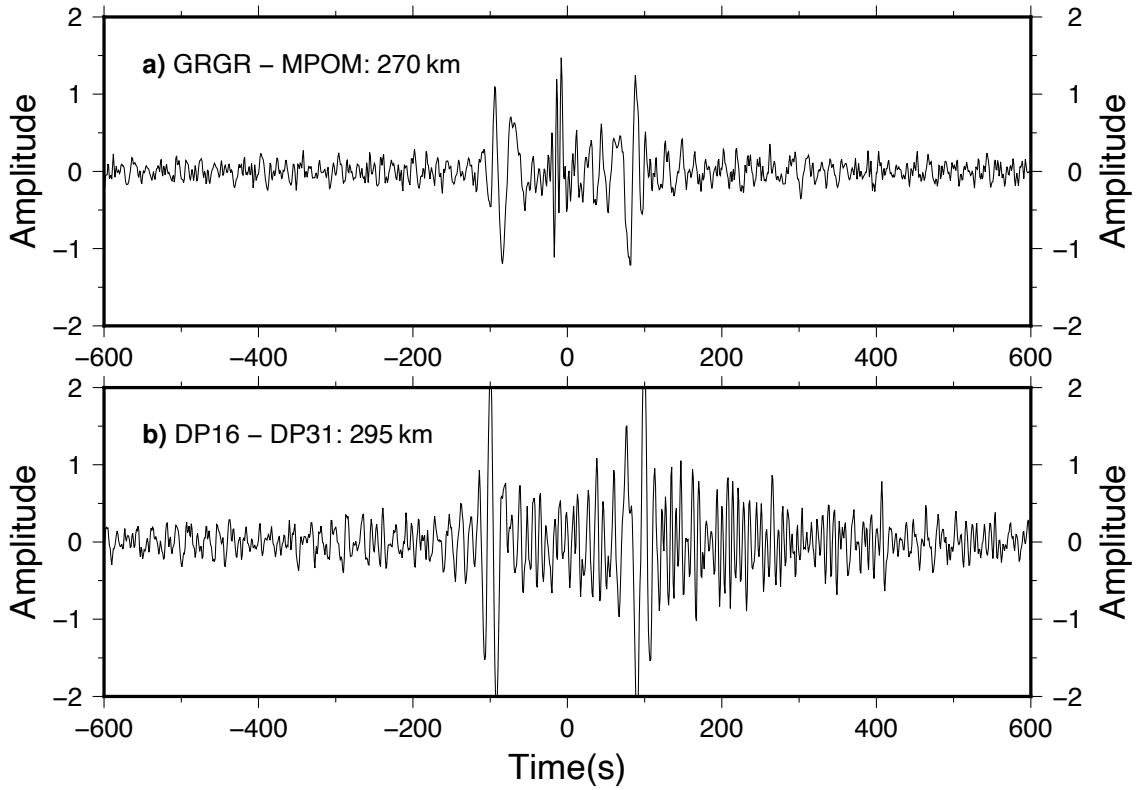

172

173 *Figure 3: Examples of 1-year symmetric vertical-vertical component cross-correlations of island*
174 *stations (a) and temporary VoiLA OBS (b). The additional peak in (a) around 0 s is likely a*
175 *processing artifact as a result of data gaps in the land station data (whereas OBS data are*
176 *continuous without gaps) and does not affect the tomography results. For the corresponding*
177 *station–station paths see Figure 1.*

178

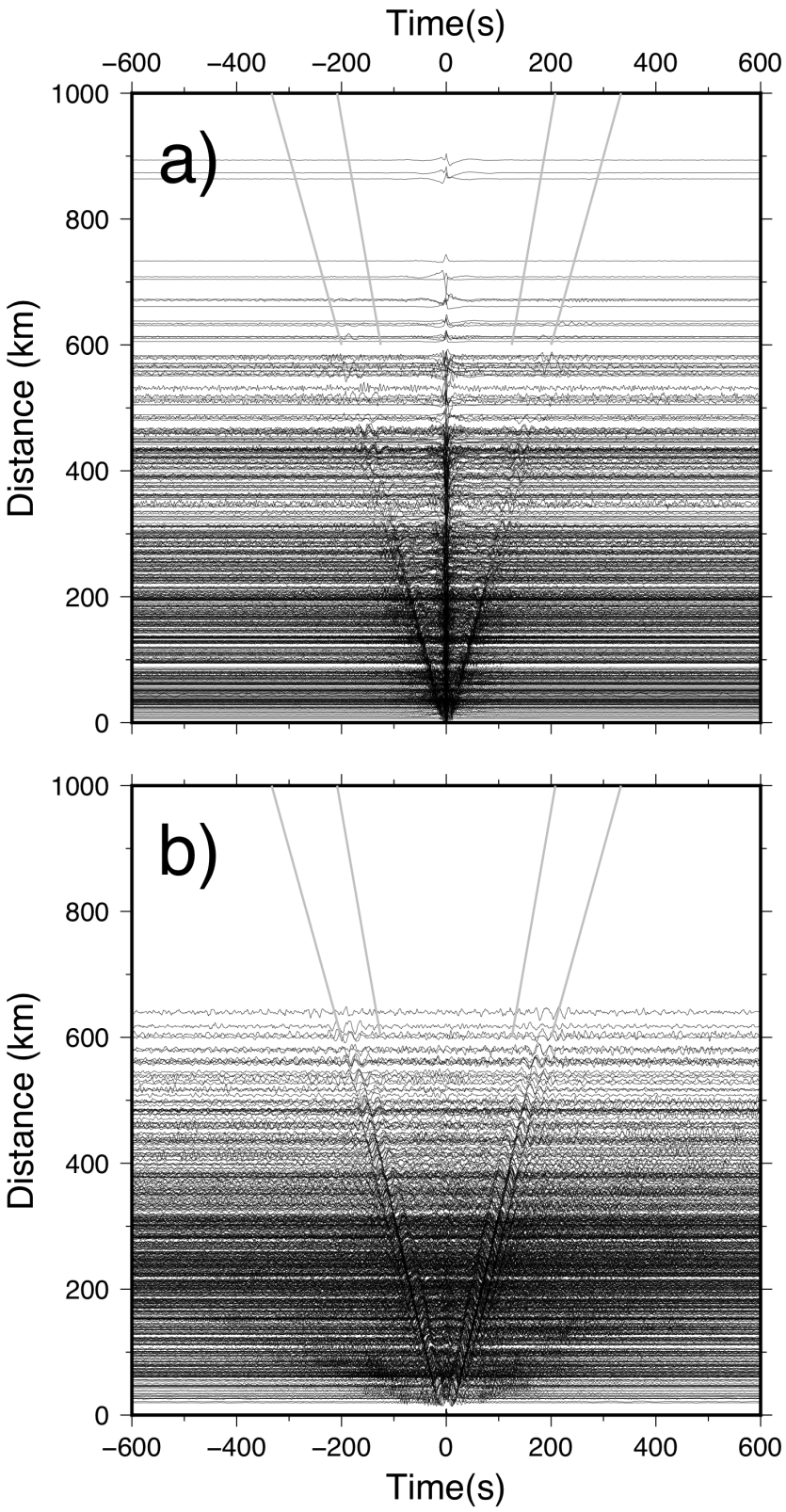

Figure 4: see following page for caption. (Please be aware that this is a version with compressed quality for the Word document.)

Figure 4: Symmetric cross-correlations of the vertical-vertical component of all station pairs ordered by station distance for the island stations (a) and the VoiLA OBS (b). The data are bandpass filtered using a 4th-order Butterworth bandpass filter between 1.5 s and 50 s. The Rayleigh waves can be seen with linear moveouts. The cross-correlation of the island stations introduces large peaks at around 0 s (a) due to data gaps in the land station data (whereas the OBS data are continuous without gaps). The cross-correlated data of the OBS shows a higher amount of noise in the codas (further away from 0 s than the Rayleigh wave onsets; b). However, these features do not affect the measurements, since we are focusing on onsets in a window around the Rayleigh wave arrivals using a search window from 3.0 km/s to 4.8 km/s. The search window is indicated by grey lines beyond a distance of 600 km. A version focusing on the first 300 km can be found in Supplementary Figure S1.

We use ambient noise cross correlations to perform Rayleigh wave tomography across the region, following the technique laid out by Sabra et al. (2005) and Shapiro et al. (2005). We use continuous data recorded at 32 OBS stations from the VoiLA project and 39 permanent land stations (Fig. 2a; Suppl. Tab. S1). The OBS were deployed in 2016 and operational for a time span of approximately 14 months, although deployment times vary from station to station (Collier, 2017). We use data from land stations covering the same time span as the OBS network. Additional land station data were used from an interval of equal length in the years 2012/2013 to test for temporal stability. The method follows the basic processing scheme of Bensen et al. (2007) and in particular the scheme presented by Harmon and Rychert (2016).

The data are processed in 1-day windows, which allows for faster computation. Here, we concentrate on the vertical components, which show Rayleigh waves most clearly and offer the highest signal-to-noise ratio (e.g., Tanimoto, 2006; Webb, 2007; Mordret et al., 2013a). Before the noise cross-correlation functions (NCF) are generated, the data are downsampled to 1 Hz. Any mean or trend is removed from the raw traces and amplitudes are normalised by a running average filter. Spectral whitening is applied in a frequency band from 0.01 to 0.33 Hz by using the magnitudes of the smoothed Fourier coefficients of the amplitude spectrum as inverse weights for the complex spectrum, acting as a spectral normalisation (Bensen et al., 2007; Harmon et al., 2008). At this frequency band, the noise field is predominantly generated by oceanic waves and double-frequency microseism (Webb, 1998), which shows a relatively random source distribution (e.g., Harmon et al., 2008; Mordret et al., 2013b; Yang & Ritzwoller, 2008).

Station pairings for the NCFs are chosen so that their minimum distance is larger than three times the wavelength, which counteracts near-field effects, while simultaneously allowing for phases to become distinguishable (Bensen et al., 2007; Harmon et al., 2008). The interstation distance range is between 30 km and 1000 km (Figs. 3, 4). In this study we were not able to use cross-correlation of OBS data with permanent station data due to back scattering effects, multipathing and mode interference at the islands, an issue observed and discussed in previous studies (Harmon et al., 2012; Tian & Ritzwoller, 2015; see also Suppl. Fig. S2). However, both cross-correlation datasets are combined afterwards, resulting in a total number of 1906 pairs (496 OBS pairs and 1410 permanent station pairs; Fig. 2a). The 1-day NCFs for a particular station

pairing are then stacked. Due to the linearity of cross-correlation the result is the equivalent of a longer timeseries (Bensen et al., 2007).

The waveforms in the positive ("causal") and negative ("acausal") parts of the resulting vertical-vertical (ZZ) component of the NCF are equivalent to waves travelling in both directions between the stations. Summing the positive and the time-reversed negative parts results in a causal, symmetric NCF that represents an average of both parts (Bensen et al., 2007; Harmon et al., 2010; see also Figs. 3, 4). The slight asymmetric behaviour of the traces can be explained by inhomogeneous distribution of noise sources (Bensen et al., 2007; Mordret et al., 2013b), though at low frequencies this is expected to be a minor problem. We window the symmetric NCF using a Tukey window with a 40 s falloff before unwrapping the phase to determine individual cycle ambiguities (Harmon & Rychert, 2016).

To estimate the average phase velocity structure of the region we approximate the real component of the Fourier transformed NCF using Bessel functions of the first kind, representing 2-dimensional noise source distribution (Aki, 1957). Harmon et al. (2010) show that this approximation is valid at the longer periods used in this study (>7 s). The minimum variance determines the best fit and thus the best amplitude/phase velocity pair. We search for phase velocities in an interval of expected values (3.0 km/s to 4.8 km/s) and select periods ranging from 6 s to 50 s. To investigate the lateral phase velocity structure at different depths we introduce nodal parametrisation (Fig. 2b) and use 2d sensitivity kernels (Zhou et al., 2004) from the average dispersion as the background model, allowing for perturbations from the uniform model in our tomography method (Harmon & Rychert, 2016). The sensitivity kernels are averaged at the nodes using an 80 km Gaussian smoothing window for the inversion parameterization. The same smoothing window is used to perform distance weighted interpolation from the nodes after the inversion to the higher resolution grids (0.1˚ spacing) shown in the paper. In the damped iterative inversion scheme, we use a damping of 0.2 km/s for the phase velocity at each node. After the inversion we propagate the error out onto the finer grid using the full covariance matrix.

Shear-wave velocity inversions from pseudo-dispersion curves are conducted on a 0.1˚ by 0.1˚ grid throughout the region of interest. We use an iterative non-linear inversion. The starting model is built of 54 layers; the first represents a water layer with changing thickness (Becker et al., 2009); the second represents a sediment layer, again with changing thickness based on a 5x5 arc-minute global sediment thickness compilation (Divins, 2003); the remaining layers have fixed thicknesses (two 1 km layers at the top and 5 km below). All layers (except for the water layer, which has v_S=0.0 and v_P=1.5. km/s) have a v_P/v_S ratio of 1.8 as an average of the ratio that varies laterally and with depth (Schlaphorst et al., 2018). The v_S values are: 0.7 km/s for the sediments (1.5 km/s for sediment thicknesses greater than 1 km), 3 to 4 km/s in even increments in the crust, and 4.5 km/s in the mantle. The low velocity zone in the asthenospheric mantle wedge beneath 70 km improves the fit to the longer frequencies, although the change is not significant due to the low sensitivity at that depth. A low velocity zone in this region would be consistent with higher fluid and/or melt concentrations as suggested by receiver function imaging of a sharp velocity drop with depth and geochemical indicators of serpentine (Chichester et al., 2019; Cooper et al., 2020). Densities are calculated using relationships for crustal (Christensen & Salisbury, 1975) and mantle layers (Birch, 1961). We replace the water layer with the sediment values for regions above sea-level. Due to the marine environment of the region we expect low

shear-wave velocities in the upper layers, which are prone to be water saturated (Mordret et al., 2014). An upper limit for S-wave velocity of 4.5 km/s in the crust and 4.85 km/s in the mantle is fixed in the inversion. We use a normalized chi-squared value as our objective function for the inversion. In most regions, we are able to reach a normalized chi-squared value of < 1, indicated we are fitting the data within its error. This criterion is used subsequently to mask out regions without sufficient misfit reduction. The shear-wave phase velocity uncertainties are the formal errors in the model parameters from the last iteration of the linearised least squares inversion.

We examine the resolution of the phase velocity map inversion using a recovery test (Fig. 5). As input we use anomalies placed with 1˚ distance for 14 and 20 s periods and 1.5˚ distance for 30 and 45 s periods. These periods were chosen to cover the entire range used. The anomaly strength is set to ±1% around the average velocity for each period, which is a good proxy for the strength of anomalies that can be expected in this study. The synthetic phase is calculated using the finite frequency kernels from each period. We also include random noise to the synthetic data, equivalent to the amount of noise in the real data.

Checkerboard tests reveal a good recovery of features along the LAA for all periods especially inside the network, due to the dense station distribution. The resolution in the western GA is poorer due to the confined distribution of station locations along the islands (in the LAA this is greatly improved due to the inclusion of off-arc OBS data).

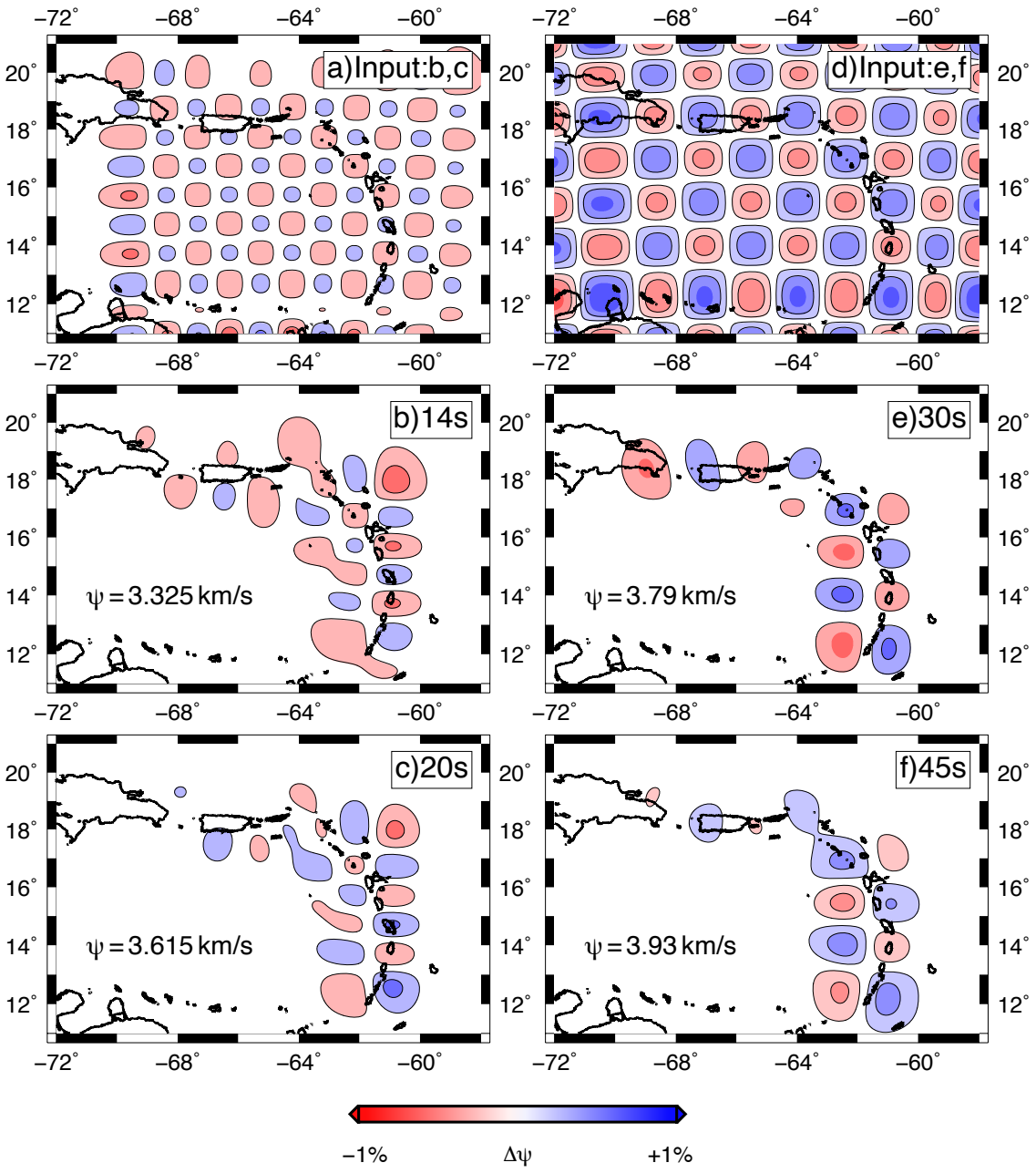

Figure 5: Recovery tests for periods shown in Figure 7. The features are placed with 1˚ distance for the shorter periods and 1.5˚ distance for the longer periods. For every period, the average velocities (here called ψ) match the ones obtained as averages of the respective periods in the real data. Note that random noise is added to the synthetic phase data, which is equivalent to the amount of noise in the real data. Further recovery tests can be found in Supplementary Figures S3–S6.

4 Results

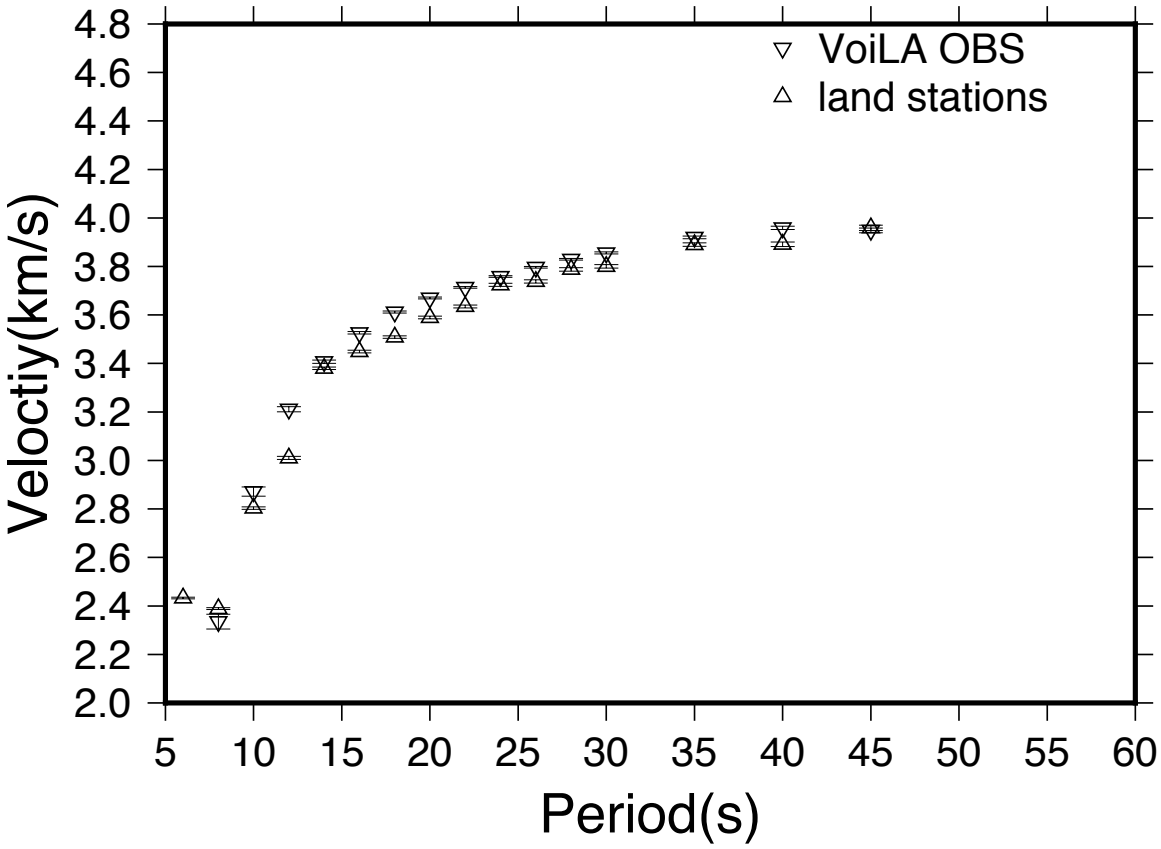

Figure 6: Measured average phase velocities and their uncertainties. Note that OBS data are systematically faster due to the different crustal properties at oceanic OBS locations.

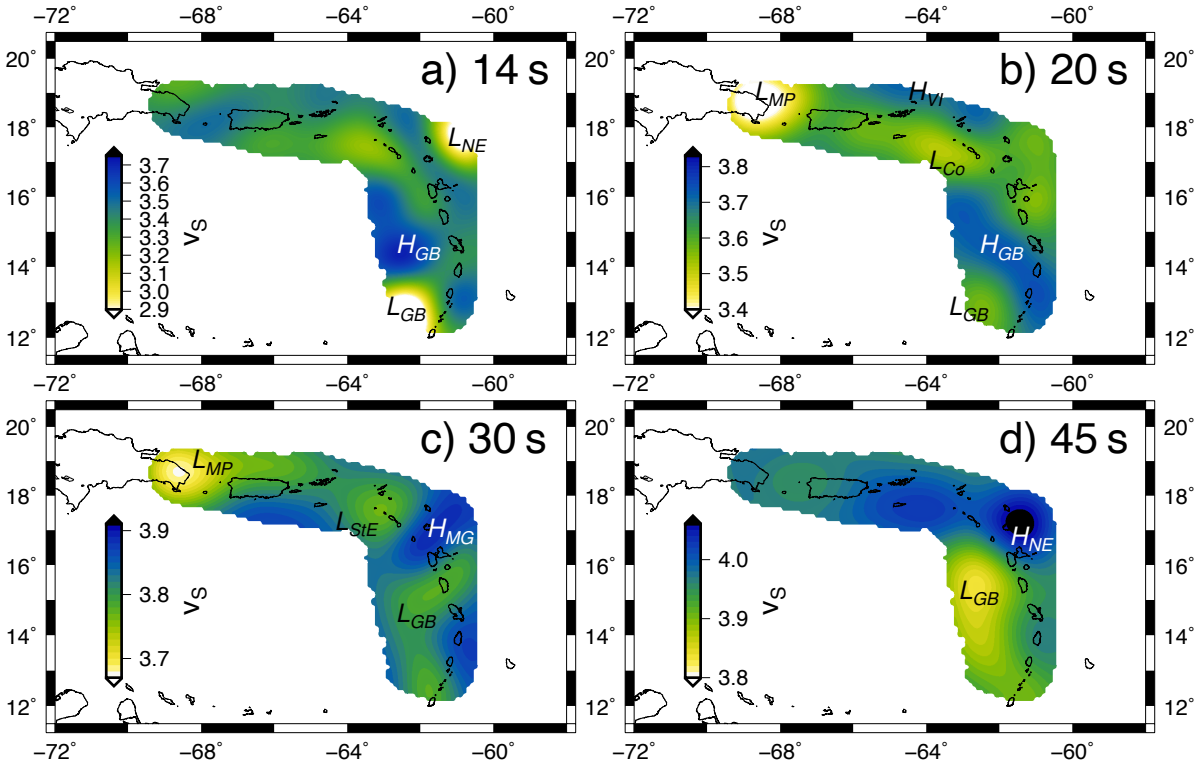

Figure 7: Surface wave tomography maps. Regions of strong low and high velocity anomalies are labelled and are discussed in the text. Phase velocity uncertainties can be found in Supplementary Figure S7.

The average phase velocities determined from the OBS and land stations (Fig. 6) show good agreement at most periods, with the dispersion recorded by the OBS being slightly faster (up to 0.05 km/s). Both dispersion curves show a steeper velocity gradient at shorter periods, reaching a plateau at longer periods that are sensitive to the upper mantle. At periods shorter than 14 s the agreement is worse at many individual grid points. This is likely due to the OBS data sensing inherently different structure from both the fore- and back-arc and rapid variation in water depth. We therefore exclude these periods in the following analysis and concentrate on the longer periods from 14 s to 45 s. To keep the approach unbiased, we keep this range for every point of the study area.

Phase velocity maps for different periods generated from the combined dataset of permanent and OBS stations are shown in Figure 7. Note that the smaller distance to the nodal border in the south does not affect the recovery of the phase velocity. At 14 s the average Rayleigh wave phase velocity for the GA and the LAA is around 3.3 km/s (Figs. 6, 7a). Two strong low-velocity anomalies can be observed in the southern Grenada Basin (L_{GB}; 2.56 ± 0.08 km/) and northeast of the northern end of the LAA (L_{NE}; 2.78 ± 0.09 km/s), which are influenced by the recovery in those regions. Furthermore, a large region of high velocities of up to 3.71 ± 0.06 km/s show in the northern part of the Grenada Basin (H_{GB}).

At 20 s the average Rayleigh wave phase velocity for the GA and the LAA is around 3.6 km/s (Figs. 6, 7b). An elongate high-velocity anomaly can be identified, which spans the area

north of the Grenada Basin, a continuation of the high-velocity anomalies observed at 14 s, and meets the LAA around St. Lucia and St. Vincent, where it reaches phase velocities of up to 3.75 ± 0.07 km/s (H_{GB}). This creates a tripartite pattern along the arc with higher velocities in the centre and significantly lower values to the north (Martinique to Saba) and to the south (the Grenadines and Grenada). A further smaller high-velocity anomaly is located north of the Virgin Islands, with phase velocities of up to 3.72 ± 0.10 km/s (H_{VI}). Three major low-velocity anomalies can be identified. One is located at the eastern end of Hispaniola at the beginning of the Mona Passage and shows phase velocities as low as 3.33 ± 0.08 km/s (L_{MP}). Two further minor low-velocity anomalies with phase velocity values of around 3.4 km/s are visible in the back-arc corner between the GA and the LAA (L_{Co}; 3.51 ± 0.08 km/s) and the southern LAA back-arc (L_{GB}; 3.56 ± 0.08 km/s).

At 30 s the average phase velocity value is 3.8 km/s (Figs. 6, 7c). The strong low-velocity anomaly beneath eastern Hispaniola also stands out at this period (L_{MP}; 3.68 ± 0.07 km/s). Along the LAA, a patchy pattern is observable with low-velocity anomalies in the north around St Eustatius (L_{StE}; 3.77 ± 0.07 km/s), as well as the centre around Dominica (3.78 ± 0.04 km/s) and in the south around Grenada (3.78 ± 0.08 km/s), the latter two being connected via the Grenada Basin (L_{GB}). These three lows are intercepted by areas of high-velocity anomalies around Montserrat to Guadeloupe (H_{MG}; 3.89 ± 0.05 km/s), as well as Martinique to St. Vincent (H_{MStV}; 3.87 ± 0.08 km/s).

At 45 s the average phase velocity value is 3.9 km/s around the LAA with slightly higher values of 4.0 km/s in the GA (Figs. 6, 7d). A round area of high velocity can be observed in the north-eastern part of the LAA (H_{NE}; 4.08 ± 0.05 km/s). In the west of the LAA a low-velocity anomaly is located in the southern two-thirds of the Grenada Basin (L_{GB}; 3.83 ± 0.06 km/s). The feature is in a similar location as the low velocity region at 30 s. The area north of Guadeloupe consistently shows higher average shear-wave velocities under the arc with the feature extending to western Puerto Rico.

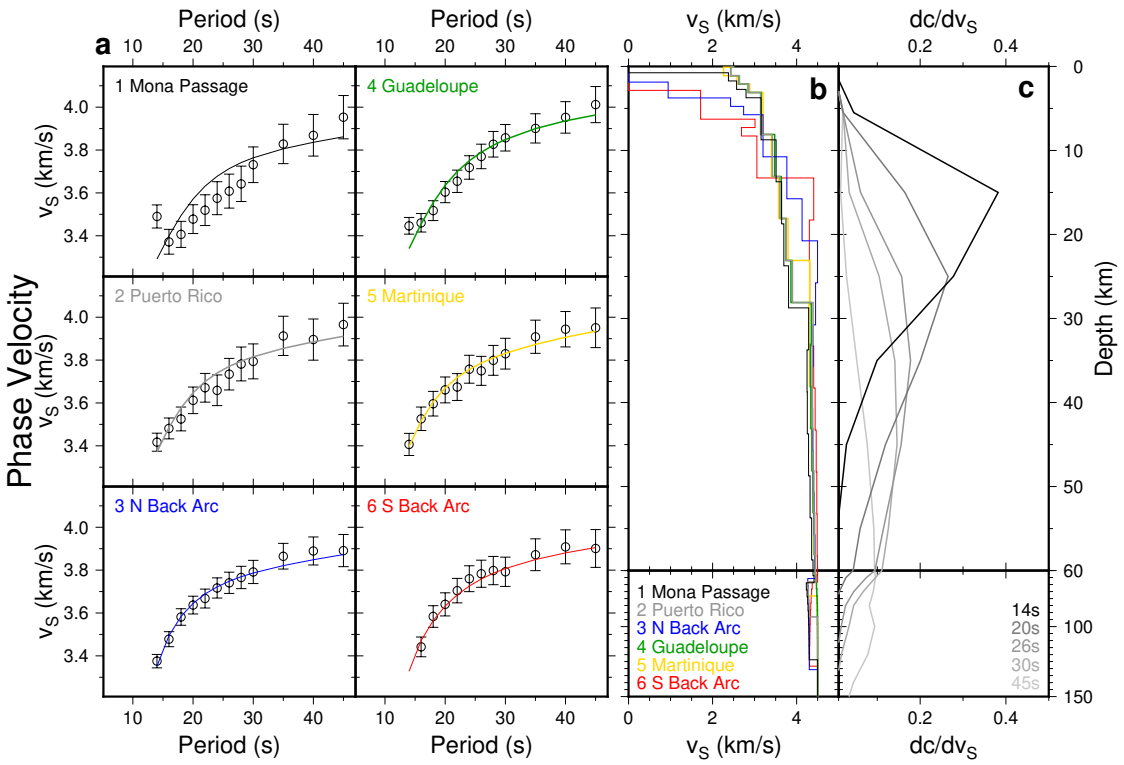

Figure 8: Dispersion results for 6 locations around the GA (Mona Passage, Puerto Rico) and LAA (Northern Back-arc, Guadeloupe, Martinique, Southern Back-arc). The locations are indicated in Figure 1. (a) Model of shear velocity dispersion curve (line) based on 1-D phase velocity estimates (black circles with error bars). (b) Resulting best fit shear velocity model. (c) Rayleigh wave sensitivity kernels with depth at different periods with c representing the model phase velocity (Zhou et al., 2004). Note that the depth scale is condensed below 60 km.

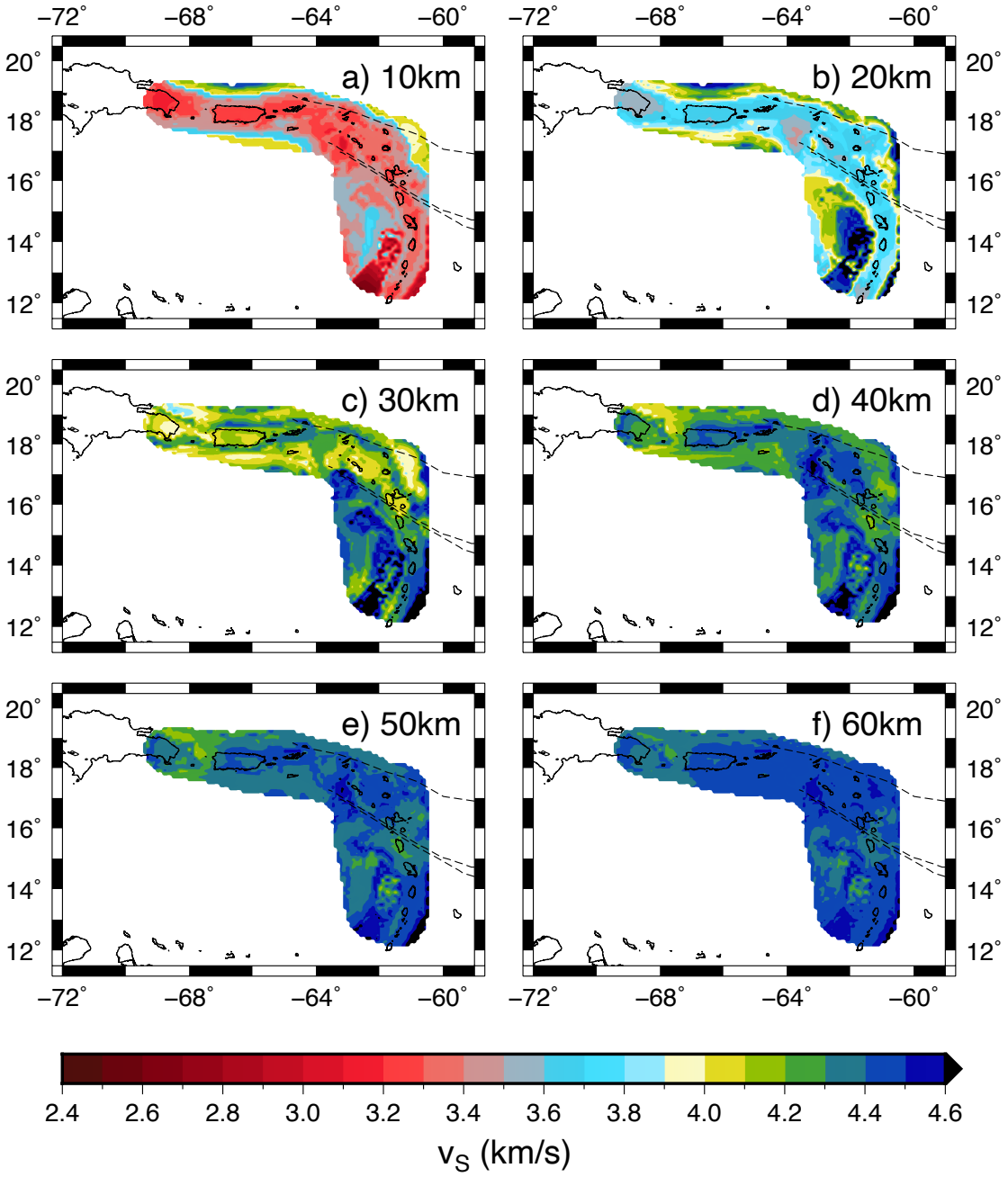

356

357 *Figure 9: S-wave velocity depth slice maps in the GA and the LAA. The red-to-light blue scale*
358 *indicates S-wave velocities commonly associated with crustal values, whereas the yellow-to-*
359 *dark-blue scale indicates values associated with mantle values. White areas depict regions*
360 *without results, due to either a high misfit in the inversion or location with great distance from*
361 *the station pair paths (see Fig. 2a). Thin black hashed lines indicate fracture zones (Cooper et*
362 *al., 2020). Note that based on our resolution tests, we do not interpret features smaller than 50*
363 *km, which are influenced by small-scale variations in water depth and sediment thickness.*

364

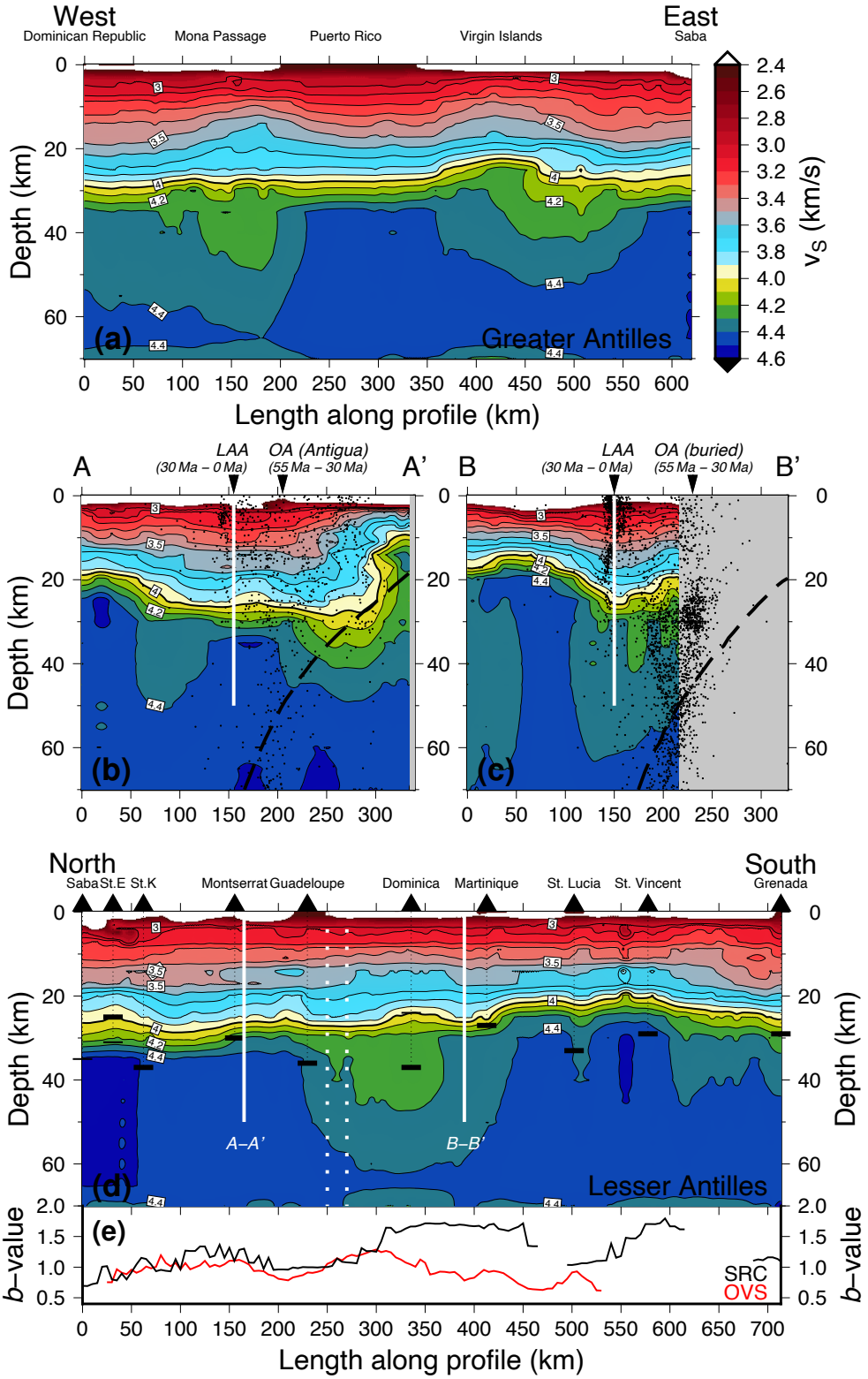

365

366 *Figure 10: see next page for caption.*

Figure 10: Velocity–depth transects along the GA (a), across the LAA (b,c), and along the LAA (d), including b*-values along the arc (e). The transect crossing positions are marked by white vertical bars. See Figure 1 for line locations. The black dots in (b,c) show all seismicity in a 30 km distance to the transect, based on the catalogue of the Institut de Physique du Globe de Paris (IPGP) from the years 1996 to 2012 and events located with the VoiLA OBS network (Bie et al., 2020). The black dashed line show the location of the subducting slab based on slab2 (Hayes et al., 2018). The black inverted triangles show the positions of the LAA and the OA as the Limestone Caribbees in the north (b) and the buried OA in the south (c). The black vertical dotted lines with black horizontal bars indicate the Moho depth estimates based on Melekhova et al. (2019, thick bars), and Schlaphorst et al. (2018, thin bars) at stations where the former study did not provide results (Saba) or where the difference between both studies is greater than 1 km (St. Eustatius, Dominica). The approximate location of two major subducted fracture zones (see Figs. 1, 9) is bounded by vertical white dotted lines; uncertainties arise due to the oblique subduction angle. Lack of data results in the grey-shaded black under the western part of the crosscutting transects. The two along-arc* b*-value profiles show two different seismic catalogues (OVS – Observatoires Volcanologiques et Sismologiques of the Institut de Physique du Globe de Paris; SRC – Seismic Research Centre of The University of the West Indies) and are taken from Schlaphorst et al. (2016), see that study for further calculation details.*

Individual dispersion curves and shear velocity depth-velocity profiles (Fig. 8a,b) are highly variable depending on location. Below the arc, the shear-wave velocity generally increases from 2.5 km/s at depths shallower than 5 km to values around 4.5 km/s at depth of 25 – 35 km. In contrast, below the fore- and back-arc, the velocities are slower velocities down to a depth of approximately 15 km. Below this depth however, velocities in the back-arc exceed the arc values, already reaching 4.5 km/s, the average value at the bottom of the model (150 km), at this depth in the southern back-arc. The pattern changes in the Mona Passage, where the shape of the velocity increase is more gradual throughout. However, the fact that the corresponding dispersion curve does not match the phase velocities within error, likely disturbed at the short-period end (14 s), points to greater and perhaps unresolved complexity in the region (Fig. 8a).

Shear velocity depth slices (Fig. 9), and along- and across-arc transects (Fig. 10) show significant changes in the crust and upper mantle. The scale used (red – light blue and afterwards yellow – green – dark blue) indicates the values typically associated with crustal (up to 3.9 km/s) and mantle (greater than 4.0 km/s) shear-wave velocity values with a light yellow layer in between to make the separation visible.

The crust is thicker beneath the GA and the LAA and thinner in the fore- and back-arc regions (Fig. 9b). Furthermore, low-velocity anomalies at 20 km can also be found beneath the Aves Ridge, the remnant volcanic arc to the west of the back-arc region behind the Grenada Basin (see Fig. 1). In the southern basin, shear-wave velocity values are among the lowest of the entire study area (down to 2.58 ± 0.07 km/s) at 10 km depth but increase rapidly with depth to values among the highest at 20 km depth (up to 4.85 ± 0.04 km/s), also observable in the individual profiles (Fig. 8b). Around 30 km depth, the GA and the northern LAA show significantly lower velocity values compared to the southern LAA (4.0 – 4.2 km/s against 4.1 –

4.5 km/s; Fig. 9c). At greater depths, the area around the central LAA (roughly Guadeloupe to Martinique) shows decreased velocities to the surrounding LAA (Fig. 9d–f).

This north-south division of the LAA is also apparent in the along-arc transect, with the island of Dominica roughly marking the change (Fig. 10d). The arc crust is on average 5 km thinner in the south (20 – 25 km vs 25 – 30 km). At 10 km depth, lower velocities can be found beneath the islands in the north (Saba, St. Eustatius, St. Kitts) and the south (Grenada). In contrast, the lowest velocities at around 30 to 40 km depth can be found beneath the islands towards the centre of the arc (especially Dominica, but also Guadeloupe; Fig. 10d).

Transects crosscutting the LAA (Fig. 10b,c) generally show thicker crust beneath the arc. In the north around Montserrat the thickened crust persists many tens of kilometres into the fore- and back-arc (Fig. 10b), whereas in the central arc around Martinique the thinning occurs more abruptly (Fig. 10c). There, a low velocity region (v_S < 4.3 km/s) is apparent below 70 km creating the mantle wedge. In the cross sections the majority of crustal seismicity above the slab matches the crustal thickness derived from the tomography values (Fig. 10b,c). Furthermore, towards the forearc seismic velocities at depths between 30 km and 55 km are lower in the central arc (4.2 – 4.4 km/s) than in the northern part (4.3 – 4.5 km/s).

In the eastern part of the GA (Fig. 10a) the depth-velocity profile resembles that in the northern LAA. Mantle values around 40 km depth are higher beneath Puerto Rico, comparable to the northern and southern LAA, whereas to the west (Mona Passage, Hispaniola) and the east (Virgin Islands) the subsurface structure profile resembles more the pattern observed in the central part of the LAA.

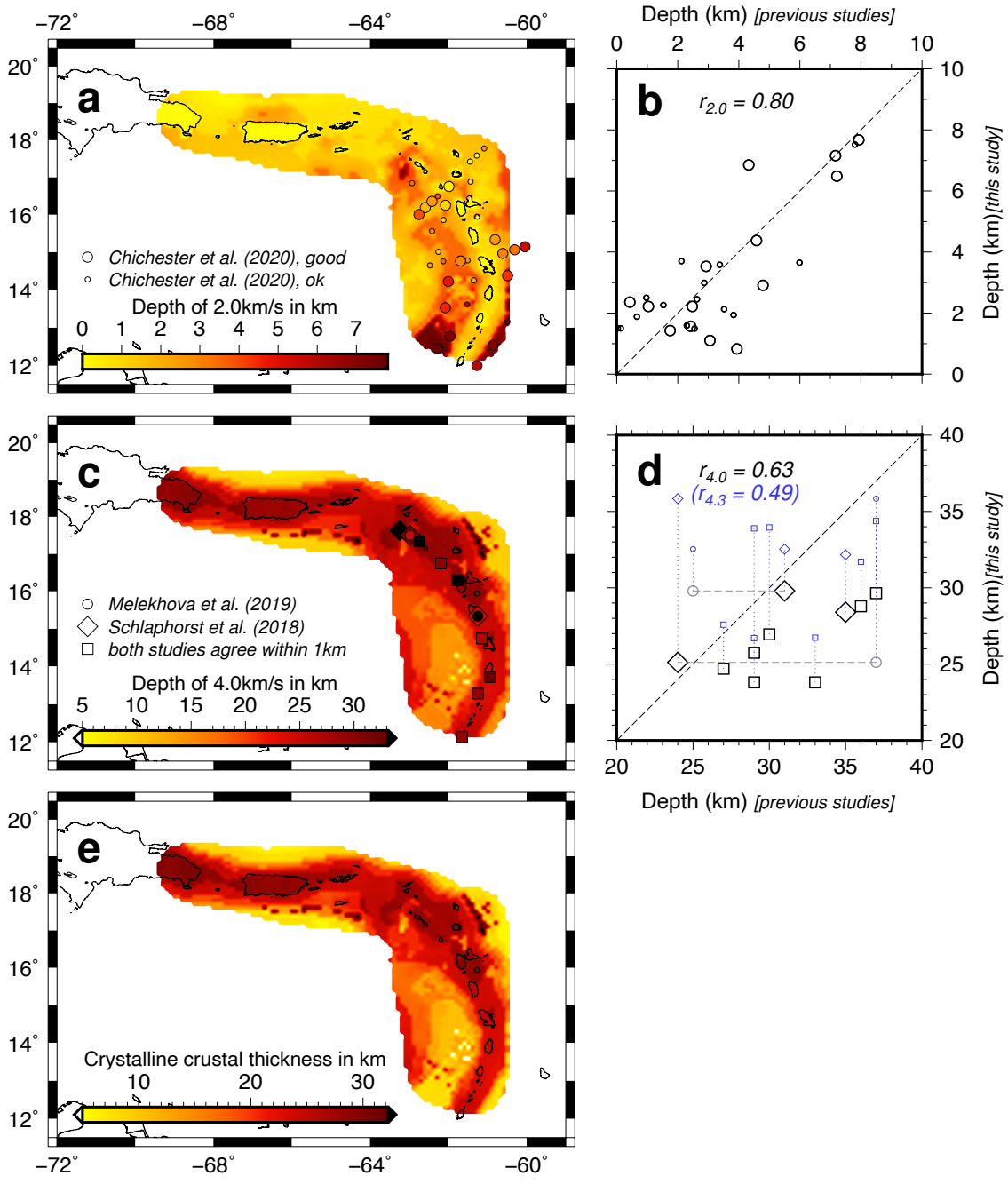

Figure 11: see next page for caption.

Figure 11: Equivelocity surfaces to map sediment layer depth and Moho depth. a) Depth of 2.0 km/s surface as an estimate of sediment limit. Circles represent depth estimates from previous study (Chichester et al., 2020), the size represent quality of the results. b) Pointwise comparison between previous and current studies, also showing the correlation coefficient ($r_{2.0}$). c) Depth of 4.0 km/s surface as an estimate of Moho depth. Diamonds, circles and squares represent depths from previous studies (Schlaphorst et al., 2018; Melekhova et al., 2019). d) Pointwise comparison between previous and current studies, also showing the correlation coefficient ($r_{4.0}$). Note that for two measurements Moho depth estimates between both previous studies differ significantly. In those cases both symbols are plotted and connected with grey hashed line. The depths of the 4.3 km/s surface at the same points are indicated by smaller blue symbols, connected by blue dotted lines and their correlation coefficient is shown in blue ($r_{4.3}$). e) Crystalline crustal thickness, calculated from difference between depths of 4.0 km/s and 2.0 km/s surfaces.

Our result may also be used to specifically map sediment and crustal thickness (Fig. 11). We choose average proxy values that are typically associated with the base of the sediment layer (2.0 km/s; Fig. 11a) and the location of the Moho (4.0km/s; Fig. 11c). We acknowledge that slightly different choices, such as gradients or other nominal velocity values are possible, but our choices compare well with estimates from previous studies of sediment thickness (Chichester et al. 2020; circles in Figs. 11a,b) and the Moho depth (Schlaphorst et al., 2018; Melekhova et al., 2019; symbols in Fig. 11c,d). Resolution in the shallowest parts of the model is diminished (Fig. 8c) and may partially explain the good correlation with sediment structure that was an input of the starting model. However, we do observe changes from the start model at these depths that improve the fit to the data.

The depth to the 2.0 km/s velocity contour shows thick sedimentary loads (Fig. 11a) in the area around the southern LAA in the fore-arc (Tobago Basin) and back-arc regions (Grenada Basin) with values exceeding 7 km. In the back-arc the extent of the deepened 2.0 km/s velocity contour in the Grenada Basin can be observed as far north as the region west of Guadeloupe. There however, the sedimentary thickness decreases to values of around 4 km. The northern part of the LAA, as well as the entire GA show thinner sedimentary thicknesses, generally not exceeding 2 km. Thinner sedimentary thicknesses of less than 1 km are observed right on the Aves Ridge, the LAA and the continuation into the GA.

The depth to the 4.0km/s velocity contour shows the deepest values on the LAA and the GA (Fig. 11c) with values exceeding 25 km. The LAA shows consistently deeper values in the northern part (north of Dominica). Together with Hispaniola and the Mona Passage, the depths can be observed to reach 30 km there. In contrast, the fore- and back-arc basins show significantly shallower depths at values below 15 km, especially in the southern and central Grenada Basin.

Differencing the 4.0 km/s and the 2.0 km/s surfaces, we can calculate an estimate for the crustal thickness (Fig. 11e). The resulting map clearly shows the thicker crustal areas of the LAA, the GA and the Aves Ridge and the thinner crustal areas with minimum values reaching 10 km in the fore- and back-arc with the Grenada Basin again being the most pronounced.

Maximum values reach 30 km in the northern LAA and parts of the GA and are slightly lower at around 25 km in the southern LAA and the Aves Ridge.

5 Discussion

The shear-wave velocity structures of the eastern GA and the LAA observed in this study reveal the variations in sediment and crustal thickness across the region. These results yield insights into the construction of the arc and adjacent basins, especially its tectonic history in terms of arc jumps and the influence of fracture zones and sediment subduction on the along-arc heterogeneity.

The sediment thickness we infer from the 2 km/s contour map in this study is thicker in the south in both the Grenada Basin and Tobago Basin near the South American Margin (Fig. 11a). The thickness is in general agreement with point measurements derived from scattered phases and refraction work in the region (Allen et al., 2019; Chichester et al., 2020; Padron et al., 2020), showing a correlation coefficient of $r = 0.80$, which gives confidence in the choice of this velocity as our estimated proxy (Fig. 11b). The thickening of sediment load is consistent with high sediment output from the Orinoco river and active back-arc spreading in the Paleogene (Allen et al., 2019).

In a similar way, there is general agreement between the 4.0 km/s contour depth and the crustal thickness values derived from receiver function studies and petrological constraints (Fig. 11c; Schlaphorst et al., 2018; Melekhova et al., 2019). The southern sub-arc crust is thinner than that in the north in all models (Melekhova et al. 2019; Schlaphorst et al., 2018). The trend in our result is more pronounced than that of the receiver function study, and the absolute depths of our study, based on the 4.0 km/s contour, is smaller than those from receiver functions (Fig. 11d). This is likely explained by the difference in calculation method. Receiver functions are based on relative velocity contrasts at a single point measured with phases with almost vertical incidence angles, whereas ambient noise tomography is averaged over a larger inter-station area, thus having broader lateral sensitivity. In addition, the absolute depth of the surface wave derived Moho is not well resolved owing to trade-off with velocities above and below the contour. Still, the correlation coefficient of $r = 0.63$ hints to a positive correlation. We also compare previous results to the 4.3 km/s contour, which increases our inferred Moho depth, but also decreases the correlation coefficient (Fig. 11d). In addition, the thicker crust in the Aves Ridge and thinner crust in the Grenada and Tobago Basins (22 km vs < 10 km) agree with values found by an active source wide angle seismic profile experiment across the region (Christeson et al., 2008).

The variations in crustal thickness are likely related to the complex tectonic setting with multiple subduction fronts at the edges of the microplates in the GA, with active and relict parts of the arc in near proximity (Boschman et al, 2014). Thicker crust beneath the LAA and GA arc platforms, in comparison to areas surrounding the arc, is consistent with the notion of magmatic addition to the top and base of the Caribbean crust due to arc volcanism (Fig. 11c,e). Variation within the arc platform, e.g. the northern LAA is thicker than the Southern LAA, is likely due to the presence of the OA, which was active 55 to 30 Ma when the Grenada Basin was opening in the south (Allen et al., 2019). In other words, the arc platform in the northern LAA is thicker due to more sustained, but laterally varying arc volcanism (Wadge, 1984). The crystalline crustal thickness inferred by differencing the depth between the 2.0 km/s and 4.0 km/s contour in the

southern Grenada and Tobago Basins implies southward thinning to < 8 km (Fig 11e). This is consistent with past back-arc extension until ~8 Ma (Allen et al., 2019). The northern part of the Grenada Basin appears to be made of stretched arc material with no back arc spreading, leading to the bulbous shape of the OA in the south LAA and larger distances between the LAA and the OA. This pinning of the arc position in the north was due to differential boundary forces with the American plates (Figs. 1,10B,C; Allen et al., 2019; Padron et al., 2020).

Velocity variations at 30 to 60 km depth, which we interpret to be the upper mantle, are in general agreement with previous results. The pronounced section of low velocity (< 4.4 km/s) beneath Guadeloupe to Martinique is consistent with noise tomography using the permanent land stations (Arnaiz-Rodríguez et al., 2020) and also the teleseismic study using the same data set used here (Cooper et al., 2020).

Variations in upper plate mantle velocities also reveal additional insight into the dynamics of the system and in particular the relationship between the wedge and arc volcanism. Slow velocities beneath the north-central arc (Guadeloupe, Dominica and Martinique) at 30 to 60 km depth, and to a lesser extent beneath the Grenadines and Grenada at 30 to 40 km are all located in regions of thickened crust, interpreted based on the 4.0 km/s velocity contour. These anomalies could be caused by upwelling of hot mantle material and/or a small amount of partial melt and fluids, potentially caused by flux melting and/or decompression melting. The along-arc heterogeneities are observed on small length scales (tens of kilometres), which is also observed in changes of characteristics such as mantle xenolith mineral composition (Melekhova et al., 2019).

The low-velocity zone in the mantle wedge beneath Guadeloupe and Martinique is bounded by two major fracture zones to the north, which also lie near the boundary of the proto-Caribbean/equatorial Atlantic seafloor boundary (Cooper et al., 2020; Harmon et al., 2019). The *b*-values of slab earthquakes (Schlaphorst et al., 2016) are also higher in the forearc offshore of Dominica and Martinique, in close proximity to our seismic anomaly, suggesting greater fluid release in this part of the subduction zone. The higher *b*-values also coincide with a region of lower seismic velocity on the slab from local earthquake and active source tomography (Paulatto et al., 2017). The high $\delta^{11}B$ anomaly in erupted magmas from Guadeloupe and Dominica, indicative of dewatering of serpentinized oceanic crust, occurs just north of that region, closer to the fracture zones on the slab in the north that bisect Guadeloupe and Martinique (Cooper et al., 2020). In addition, pre-existing faults from the formation at the ridge can open via bending during the subduction process, thus allowing for further hydration. However, the lack of intraslab, trench-parallel normal fault focal mechanisms from earthquakes in the forearc and outer rise makes this process unlikely to have a dominant role. An alternative explanation is that there is three-dimensional flow owing to the curvature of the arc or gaps in the slab (e.g., Harris et al., 2018; Schlaphorst et al., 2017), which can have an effect on the lateral placement and extension of the anomaly to the south of the fracture zones. Similarly, ponding melt could redistribute fluids and/or melt between the slab and the arc (Ha et al., 2020). Linked to that, the most productive volcanoes over the last 100 kyr can be found on Dominica (Wadge, 1984). Another possibility is that along-strike variability in the morphology of the subducted seafloor itself can have an impact on the velocity structure of the mantle wedge and the upper plate. For instance, oceanic core complexes, that are formed in slow- and intermediate-spreading environments, at times when magma supply is limited (Smith et al., 2008) may cause crustal

alteration, based on slow seismic velocities outboard on the incoming plate of our study area (Davy et al., 2019).

Further north, the lower velocities throughout the upper mantle between Hispaniola and Puerto Rico (Fig. 10a) occur in a region with moderate interpreted crustal thickness (close to 30 km). The anomaly is interesting and potentially different to the rest of the arc where low upper mantle velocities are associated with thickened crust and an active volcanic arc. This anomaly could arise due to the ongoing opening of the Mona Passage (Jansma et al., 2005). In other words, the extensional tectonics may cause upwelling of hotter, potentially more hydrated mantle material from depth, possibly also associated with decompression melting.

6 Conclusions

In this study we used ambient noise tomography to map crustal and upper mantle shear-wave velocity of the eastern GA and the LAA using data from permanent land stations and from ocean bottom seismometers collected as part of VoiLA experiment in 2016/17. We observe significant along-arc heterogeneities on small length scales (~50 km) that agree with heterogeneities of a variety of characteristics such as mantle xenolith mineral composition and discontinuity structure (including crustal thickness) variation, changes in sediment and water subduction, as well as melt generation distribution observed by previous studies. Our estimates of sedimentary basin and crustal thickness agree with point measurements and profiles throughout the LAA from previous modelling of receiver functions, petrology, and active source studies. We observe increased sediment thickness (> 7 km) in the southern fore- (Tobago Basin) and back-arc regions (Grenada Basin). This can be explained by sediment supply from the Orinoco and active back-arc spreading in the Paleogene. The crust is thicker beneath the GA and the northern LAA islands, reaching values of around 30 km. The LAA south of Dominica shows smaller crustal thickness values of 20 to 25 km. In the fore-arc, where the older arc has been buried under the thick Barbados sediments (Allen et al., 2019), and in the back-arc regions in the Grenada Basin, crustal thickness are as low as 10 km. Along the arc, shear-wave velocities in the upper mantle are significantly lower beneath the Mona Passage, as well as beneath the central LAA from Guadeloupe to Martinique (4.2 – 4.4 km/s). This can be explained by upwelling of hot mantle material or a small amount of partial melt, or both, and is likely caused by flux or decompression melting or a combination of these. The subduction of the proto-Caribbean/equatorial Atlantic seafloor boundary at two major fracture zones are located just north of the anomaly that runs from Guadeloupe to Martinique. Therefore, three dimensional flow because of slab curvature and/or a gap in the slab, seafloor morphology such as oceanic core complexes, and/or melt ponding with potential influences from the overriding plate (or a combination of those) are likely to have a dominant impact on the location and degree of arc volcanism in the area. In general, slow spreading ridges, in our case the MAR, lead to high amount of hydration with high along-arc variability. This results in the slow subduction of highly heterogeneous slab hydration patterns that facilitate the variable crustal and upper mantle structure we observed.

Acknowledgments, Samples, and Data

We would like to thank Tim Greenfield and Joshua Russel for their constructive comments and suggestions. This research was funded by the VoiLA NERC consortium grant (NE/K010824/1). We thank all who sailed on cruises RRS James Cook JC133 and JC149. We thank our partners at the University of West Indies Seismic Research Centre (SRC), in particular Lloyd Lynch, Kemron Alexander, Richard Robertson and Joan Latchman as well as Laura Petrescu and Ben Chichester for support with island station installation, the German Instrument Pool for Amphibian Seismology (DEPAS), hosted by the Alfred Wegener Institute Bremerhaven for providing the ocean-bottom and temporary island seismometers, and UCSD (Scripps) for providing additional ocean-bottom seismometers. DS would like to acknowledge the financial support FCT through project SIGHT (Ref. PTDC/CTA-GEF/30264/2017) and UIDB/50019/2020 – IDL. Data used in this project are available from the IRIS DMC (www.iris.edu/dmc) and we used of data from the following Networks: CU (https://doi.org/10.7914/SN/CU), G (https://doi.org/10.18715/GEOSCOPE.G), IU (https://doi.org/10.7914/SN/IU), NA (https://doi.org/10.21944/dffa7a3f-7e3a-3b33-a436-516a01b6af3f), PR (https://doi.org/10.7914/SN/PR), TR (No Doi), WI (https://doi.org/10.18715/antilles.WI), and XZ (https://doi.org/10.7914/SN/XZ_2016). Results of this work are stored in a repository (https://doi.org/10.5281/zenodo.4994770)

References

Allen, R. W., Collier, J. S., Stewart, A. G., Henstock, T., Goes, S., Rietbrock, A., & VoiLA Team. (2019), The role of arc migration in the development of the Lesser Antilles: A new tectonic model for the Cenozoic evolution of the eastern Caribbean. *Geology*, 47(9), 891–895. doi: 10.1130/G46708.1

Aki, K. (1957), Space and time spectra of stationary stochastic waves, with special reference to microtremors. *Bulletin of the Earthquake Research Institute*, 35, pp.415-456.

Arnaiz-Rodríguez, M. S., Schmitz, M., & Audemard, F. (2016), La estructura cortical del arco de las Antillas Menores estimada a partir de la técnica de funciones receptoras. *Revista mexicana de ciencias geológicas*, 33(3), pp.286–296.

Arnaiz-Rodríguez, M. S., Zhao, Y., Sánchez-Gamboa, A.K., & Audemard, F. (2020), Crustal and upper-mantle structure of the Eastern Caribbean and Northern Venezuela from passive Rayleigh wave tomography. *Tectonophysics*, p.228711. doi: 10.1016/j.tecto.2020.228711

Becker, J. J., Sandwell, D. T. , Smith, W. H. F., Braud, J., Binder, B., Depner, J., et al. (200), Global Bathymetry and Elevation Data at 30 Arc Seconds Resolution: SRTM30_PLUS, *Marine Geodesy*, 32:4, 355–371, doi: 10.1080/01490410903297766

Bensen, G.D., Ritzwoller, M. H., Barmin, M. P., Levshin, A. L., Lin, F., Moschetti, M.P., Shapiro, N.M., & Yang, Y. (2007). Processing seismic ambient noise data to obtain reliable broad-band surface wave dispersion measurements. *Geophysical Journal International*, 169(3), pp.1239–1260. doi: 10.1111/j.1365-246X.2007.03374.x

Bie, L., Rietbrock, A., Hicks, S., Allen, R., Blundy, J., Clouard, V., et al. (2020), Along-Arc Heterogeneity in Local Seismicity across the Lesser Antilles Subduction Zone from a

641 Dense Ocean-Bottom Seismometer Network. *Seismological Research Letters*, 91(1),
642 pp.237–247. doi: 10.1785/0220190147

643 Boschman, L. M., van Hinsbergen, D. J., Torsvik, T. H., Spakman, W., & Pindell, J. L. (2014),
644 Kinematic reconstruction of the Caribbean region since the Early Jurassic. *Earth-Science*
645 *Reviews*, 138, pp.102–136. doi: 10.1016/j.earscirev.2014.08.007

646 Bouysse, P., Westercamp, D. and Andreieff, P. (1986), 4. The Lesser Antilles Island Arc. In
647 *Proceedings of the Ocean Drilling Program: Scientific results* (Vol. 110, p. 29). The
648 Program.

649 Boynton, C. H., Westbrook, G. K., Bott, M. H. P. & Long, R. E. (1979), A seismic refraction
650 investigation of crustal structure beneath the Lesser Antilles island arc. *Geophysical*
651 *Journal International*, 58(2), pp.371–393. doi: j.1365-246X.1979.tb01031.x

652 Cai, C., Wiens, D.A., Shen, W. & Eimer, M., 2018. Water input into the Mariana subduction
653 zone estimated from ocean-bottom seismic data. *Nature*, 563(7731), pp.389–392. doi:
654 10.1038/s41586-018-0655-4

655 Campillo, M., Roux, P. & Shapiro, N. M. 2011. Using seismic noise to image and to monitor the
656 Solid Earth. *Encyclopedia of Solid Earth Geophysics*, pp.1230–1235.

657 Chichester, B., Rychert, C., Harmon, N., Collier, J., Henstock, T., Goes, S.D., et al. (2019),
658 Seismic imaging of the Lesser Antilles subduction zone using S-to-P receiver functions.
659 In *AGU Fall Meeting Abstracts* (Vol. 2019, pp. S53C-0521).

660 Chichester, B., Rychert, C., Harmon, N., Allen, R., Collier, J., Henstock, T., & Rietbrock, A.
661 (2020). Seafloor sediment thickness beneath the VoiLA broadband ocean-bottom
662 seismometer deployment in the Lesser Antilles from P-to-S delay times. *Geophysical*
663 *Journal International*. doi: 10.1093/gji/ggaa360

664 Christeson, G.L., Mann, P., Escalona, A., & Aitken, T. J. (2008). Crustal structure of the
665 Caribbean–northeastern South America arc-continent collision zone. *Journal of*
666 *Geophysical Research: Solid Earth*, 113(B8). doi: 10.1029/2007JB005373

667 Collier, J.S. (2017), VoiLA—Volatile recycling in the Lesser Antilles arc: RRS James Cook
668 cruise report JC149. Imperial College London, https://www. bodc. ac.
669 uk/resources/inventories/cruise_inventory/reports/jc149. pdf, pp.1–161.

670 Cooper, G. F., Macpherson, C. G., Blundy, J. D., Maunder, B., Allen, R. W., Goes, S., et al.
671 (2020), Variable water input controls evolution of the Lesser Antilles volcanic arc.
672 *Nature*, 582(7813), 525–529. doi: 10.1038/s41586-020-2407-5

673 Davy, R. G., Collier, J. S., Henstock, T. J., & VoiLA Consortium. (2020), Wide-angle seismic
674 imaging of two modes of crustal accretion in mature Atlantic Ocean crust. *Journal of*
675 *Geophysical Research: Solid Earth*, 125(6), p.e2019JB019100. doi:
676 10.1029/2019JB019100

677 DeMets, C., Jansma, P. E., Mattioli, G. S., Dixon, T. H., Farina, F., Bilham, R., et al. (2000),
678 GPS geodetic constraints on Caribbean-North America plate motion. *Geophysical*
679 *Research Letters*, 27(3), pp.437–440. doi: 10.1029/1999GL005436

Dolan, J. F., Mullins, H. T., Wald, D. J., & Mann, P. (1998), Active tectonics of the north-central Caribbean: Oblique collision, strain partitioning, and opposing subducted slabs. *Special Papers-Geological Society of America*, pp.1–62.

Faugères, J. C., Gonthier, E., Griboulard, R., & Masse, L. (1993), Quaternary sandy deposits and canyons on the Venezuelan margin and south Barbados accretionary prism. *Marine Geology*, 110(1-2), pp.115–142. doi: 10.1016/0025-3227(93)90109-9

Goes S., Collier J., Blundy J., Davidson J., Harmon N., Henstock T., et al. (2019), Project VoiLA: Volatile Recycling in the Lesser Antilles, *Eo*s, 100, ISSN:2324–9250

Ha, G., Montési, L.G., & Zhu, W. (2020), Melt Focusing Along Permeability Barriers at Subduction Zones and the Location of Volcanic Arcs. *Geochemistry, Geophysics, Geosystems*, 21(12), p.e2020GC009253. doi: 10.1029/2020GC009253

Harmon, N., Gerstoft, P., Rychert, C. A., Abers, G. A., Salas de La Cruz, M., & Fischer, K. M. (2008), Phase velocities from seismic noise using beamforming and cross correlation in Costa Rica and Nicaragua. *Geophysical Research Letters*, 35(19). doi: 10.1029/2008GL035387

Harmon, N., Rychert, C. A., & Gerstoft, P. (2010), Distribution of noise sources for seismic interferometry. *Geophysical Journal International*, 183(3), pp.1470–1484. doi: 10.1111/j.1365-246X.2010.04802.x

Harmon, N., Henstock, T., Tilmann, F., Rietbrock, A., & Barton, P. (2012). Shear velocity structure across the Sumatran Forearc-Arc. Geophysical Journal International, 189(3), 1306-1314. doi: 10.1111/j.1365-246X.2012.05446.x

Harmon, N., & Rychert, C. A. (2016), Joint inversion of teleseismic and ambient noise Rayleigh waves for phase velocity maps, an application to Iceland. *Journal of Geophysical Research: Solid Earth*, 121(8), pp.5966–5987. doi: 10.1002/2016JB012934

Harmon, N., Rychert, C. A., Collier, J., Henstock, T., van Hunen, J., & Wilkinson, J.J. (2019), Mapping geologic features onto subducted slabs. *Geophysical Journal International*, 219(2), pp.725–733. doi: 10.1093/gji/ggz290

Harris, C. W., Miller, M. S., & Porritt, R. W. (2018). Tomographic imaging of slab segmentation and deformation in the Greater Antilles. Geochemistry, Geophysics, Geosystems, 19(8), 2292–2307. doi: 10.1029/2018GC007603

Hayes, G.P., Moore, G.L., Portner, D.E., Hearne, M., Flamme, H., Furtney, M., & Smoczyk, G.M. (2018), Slab2, a comprehensive subduction zone geometry model. *Science*, 362(6410), pp.58–61. doi: 10.1126/science.aat4723

Kopp, H., Weinzierl, W., Becel, A., Charvis, P., Evain, M., Flueh, E. R., et al. (2011), Deep structure of the central Lesser Antilles Island Arc: relevance for the formation of continental crust. *Earth and Planetary Science Letters*, 304(1-2), pp.121–134. doi: 10.1016/j.epsl.2011.01.024

Jansma, P. E., Mattioli, G. S., & Mann, P. (2005), GPS results from Puerto Rico and the Virgin Islands: Constraints on tectonic setting and rates of active faulting. *Active Tectonics and Seismic Hazards of Puerto Rico, the Virgin Islands, and Offshore Areas* 385, pp. 13–30

720 Lin, F. C., Ritzwoller, M. H., & Shapiro, N. M. (2006), Is ambient noise tomography across
721 ocean basins possible?. *Geophysical Research Letters*, 33(14). doi:
722 10.1029/2006GL026610

723 Lin, F. C., Ritzwoller, M. H., Townend, J., Bannister, S., & Savage, M. K. (2007), Ambient
724 noise Rayleigh wave tomography of New Zealand. *Geophysical Journal International*,
725 170(2), pp.649–666. doi: 10.1111/j.1365-246X.2007.03414.x

726 Lin, F. C., Ritzwoller, M. H., & Snieder, R. (2009), Eikonal tomography: surface wave
727 tomography by phase front tracking across a regional broad-band seismic array.
728 *Geophysical Journal International*, 177(3), pp.1091–1110. doi: 10.1111/j.1365-
729 246X.2009.04105.x

730 Masson, D. G., & Scanlon, K. M. (1991), The neotectonic setting of Puerto Rico. *Geological*
731 *Society of America Bulletin*, 103(1), pp.144–154. doi: 10.1130/0016-
732 7606(1991)103<0144:TNSOPR>2.3.CO;2

733 Meighan, H. E., & Pulliam, J. (2013), Seismic anisotropy beneath the northeastern Caribbean:
734 Implications for the subducting North American lithosphere. *Bulletin de la Société*
735 *Géologique de France*, 184(1-2), pp.67–76. doi: 10.2113/gssgfbull.184.1-2.67

736 Melekhova, E., Schlaphorst, D., Blundy, J., Kendall, J. M., Connolly, C., McCarthy, A., &
737 Arculus, R. (2019), Lateral variation in crustal structure along the Lesser Antilles arc
738 from petrology of crustal xenoliths and seismic receiver functions. *Earth and Planetary*
739 *Science Letters*, 516, pp.12–24. doi: 10.1016/j.epsl.2019.03.030

740 Mordret, A., Shapiro, N. M., Singh, S. S., Roux, P., & Barkved, O.I. (2013a), Helmholtz
741 tomography of ambient noise surface wave data to estimate Scholte wave phase velocity
742 at Valhall Life of the FieldNoise tomography at Valhall. *Geophysics*, 78(2), pp.WA99–
743 WA109. doi: 10.1190/geo2012-0303.1

744 Mordret, A., Landès, M., Shapiro, N.M., Singh, S. C., Roux, P., & Barkved, O.I., (2013b), Near-
745 surface study at the Valhall oil field from ambient noise surface wave tomography.
746 *Geophysical Journal International*, 193(3), pp.1627–1643. doi: 10.1093/gji/ggt061

747 Mordret, A., Landès, M., Shapiro, N. M., Singh, S. C., & Roux, P. (2014), Ambient noise surface
748 wave tomography to determine the shallow shear velocity structure at Valhall: depth
749 inversion with a Neighbourhood Algorithm. *Geophysical Journal International*, 198(3),
750 pp.1514–1525. doi: 10.1093/gji/ggu217

751 Padron, C., Klingelhoefer, F., Marcaillou, B., Lebrun, J. F., Lallemand, S., Garrocq, C., et al.
752 (2018), Deep structure of the Grenada Basin from wide-angle seismic, bathymetric and
753 gravity data. *Journal of Geophysical Research: Solid Earth*, p.e2020JB020472. doi:
754 10.1029/2020JB020472

755 Ritzwoller, M. H., Lin, F. C., & Shen, W. (2011), Ambient noise tomography with a large
756 seismic array. *Comptes Rendus Geoscience*, 343(8-9), pp.558–570. doi:
757 10.1016/j.crte.2011.03.007

758 Sabra, K. G., Gerstoft, P., Roux, P., Kuperman, W. A., & Fehler, M. C. (2005), Extracting time-
759 domain Green's function estimates from ambient seismic noise. *Geophysical Research*
760 *Letters*, 32(3). doi: 10.1029/2004GL021862

761 Schlaphorst, D., Kendall, J. M., Collier, J. S., Verdon, J. P., Blundy, J., Baptie, B., et al. (2016),
762 Water, oceanic fracture zones and the lubrication of subducting plate boundaries—
763 insights from seismicity. *Geophysical Journal International*, 204(3), pp.1405–1420. doi:
764 10.1093/gji/ggv509

765 Schlaphorst, D., Kendall, J. M., Baptie, B., Latchman, J. L., & Tait, S. (2017), Gaps, tears and
766 seismic anisotropy around the subducting slabs of the Antilles. *Tectonophysics*, 698,
767 pp.65–78. doi: 10.1016/j.tecto.2017.01.002

768 Schlaphorst, D., Melekhova, E., Kendall, J. M., Blundy, J., & Latchman, J. L. (2018), Probing
769 layered arc crust in the Lesser Antilles using receiver functions. *Royal Society Open*
770 *Science*, 5(11), p.180764. doi: 10.1098/rsos.180764

771 Shapiro, N. M., & Campillo, M. (2004), Emergence of broadband Rayleigh waves from
772 correlations of the ambient seismic noise. *Geophysical Research Letters*, 31(7). doi:
773 10.1029/2004GL019491

774 Shapiro, N. M., Campillo, M., Stehly, L., & Ritzwoller, M. H. (2005), High-resolution surface-
775 wave tomography from ambient seismic noise. *Science*, 307(5715), pp.1615–1618. doi:
776 10.1126/science.1108339

777 Smith, D. K., Escartín, J., Schouten, H., & Cann, J. R. (2008), Fault rotation and core complex
778 formation: Significant processes in seafloor formation at slow-spreading mid-ocean
779 ridges (Mid-Atlantic Ridge, 13–15 N). *Geochemistry, Geophysics, Geosystems*, 9(3). doi:
780 10.1029/2007GC001699

781 Stern, R. J. (2002), Subduction zones. *Reviews of Geophysics*, 40(4), pp.3-1. doi:
782 10.1029/2001RG000108

783 Stewart, P. (2006), Interferometric imaging of ocean bottom noise. In SEG Technical Program
784 Expanded Abstracts 2006(pp. 1555–1559). *Society of Exploration Geophysicists*. doi:
785 10.1190/1.2369817

786 Ten Brink, U. (2005), Vertical motions of the Puerto Rico Trench and Puerto Rico and their
787 cause. *Journal of Geophysical Research: Solid Earth*, 110(B6). doi:
788 10.1029/2004JB003459

789 Tian, Y., & Ritzwoller, M. H. (2015). Directionality of ambient noise on the Juan de Fuca plate:
790 Implications for source locations of the primary and secondary microseisms. Geophysical
791 Journal International, 201(1), 429-443. doi: 10.1093/gji/ggv024

792 Wadge, G. (1984), Comparison of volcanic production rates and subduction rates in the Lesser
793 Antilles and Central America. *Geology*, 12(9), pp.555–558. doi: 10.1130/0091-
794 7613(1984)12<555:COVPRA>2.0.CO;2

795 Wadge, G., & Shepherd, J. B. (1984), Segmentation of the Lesser Antilles subduction zone.
796 *Earth and Planetary Science Letters*, 71(2), pp.297–304. doi: 10.1016/0012-
797 821X(84)90094-3

798 Webb, S. C. (1998). Broadband seismology and noise under the ocean. Reviews of Geophysics,
799 36(1), 105-142. doi: 10.1029/97RG02287

800 Yang, Y., Ritzwoller, M. H., Levshin, A. L., & Shapiro, N. M. (2007), Ambient noise Rayleigh
801 wave tomography across Europe. *Geophysical Journal International*, 168(1), pp.259–
802 274. doi: 10.1111/j.1365-246X.2006.03203.x

803 Yang, Y., & Ritzwoller, M. H. (2008), Characteristics of ambient seismic noise as a source for
804 surface wave tomography. *Geochemistry, Geophysics, Geosystems*, 9(2). doi:
805 10.1029/2007GC001814

806 Zhou, Y., Dahlen, F. A., & Nolet, G. (2004). Three-dimensional sensitivity kernels for surface
807 wave observables. Geophysical Journal International, 158(1), 142–168. doi:
808 10.1111/j.1365-246X.2004.02324.x